HHS Public Access

Author manuscript

J Med Virol. Author manuscript; available in PMC 2025 January 01.

Published in final edited form as:

J Med Virol. 2024 January ; 96(1): e29349. doi:10.1002/jmv.29349.

Generation and characterization of a humanized ACE2 mouse model to study long-term impacts of SARS-CoV-2 infection

Chang-Yong Choi[1,#], **Kundlik Gadhave**[2,#], **Jason Villano**[4], **Andrew Pekosz**[5], **Xiaobo Mao**[2,3,*], **Hongpeng Jia**[1,*]

[1]Division of Pediatric Surgery, Department of Surgery, Johns Hopkins University School, of Medicine, Baltimore, MD 21205, USA.

[2]Institute for Cell Engineering, Department of Neurology, Johns Hopkins University School of Medicine, Baltimore, MD 21205, USA.

[3]Institute for NanoBioTechnology, Department of Material Science and Engineering, Johns Hopkins Whiting School of Engineering, Baltimore, MD 21218, USA.

[4]Molecular and Comparative Pathobiology, The Johns Hopkins School of Medicine, Baltimore, MD 21205, USA.

[5]Department of Molecular Microbiology and Immunology, The Johns Hopkins Bloomberg School of Public Health, Baltimore, MD 21205, USA.

Abstract

Although the COVID-19 pandemic has officially ended, the persistent challenge of long-COVID or post-acute COVID sequelae (PASC) continues to impact societies globally, highlighting the urgent need for ongoing research into its mechanisms and therapeutic approaches. Our team has recently developed a novel humanized ACE2 mouse model (hACE2ki) designed explicitly for long-COVID/PASC research. This model exhibits human ACE2 expression in tissue and cell-specific patterns akin to mouse Ace2. When we exposed young adult hACE2ki mice (6 weeks old) to various SARS-CoV-2 lineages, including WA, Delta, and Omicron, at a dose of 5×10^5 PFU/mouse via nasal instillation, the mice demonstrated distinctive phenotypes characterized by differences in viral load in the lung, trachea, and nasal turbinate, weight loss, and changes in pro-inflammatory cytokines and immune cell profiles in bronchoalveolar lavage fluid (BALF). Notably, no mortality was observed in this age group. Further, to assess the model's relevance for long-COVID studies, we investigated tau protein pathologies, which are linked to Alzheimer's disease, in the brains of these mice post SARS-CoV-2 infection. Our findings revealed the accumulation and longitudinal propagation of tau, confirming the potential of our hACE2ki mouse model for pre-clinical studies of long-COVID.

*Corresponding authors xmao4@jhmi.edu; hjia4@jhmi.edu.
#These authors contributed equally

Author contributions:

CYC contributed to experimental design, implementation, data collection, and initial manuscript drafting. KG contributed to biochemical and mouse experiments. XM and HGJ designed the research wrote and revised the paper. AP contributed to viral stock generation, purification, and validation. AP also provides intellectual consultants. JV helped with ABSL3 support with the additional intellectual consultant. All authors reviewed, edited, and approved the paper.

Keywords

SARS-CoV-2; humanized ACE2 mouse model; immune response; long-COVID; Alzheimer's disease; tau pathology

Introduction

The global impact of COVID-19 has been staggering, with approximately 770 million reported infections and over 6.9 million lives lost worldwide (WHO Coronavirus Dashboard). Despite the declaration of the end of the COVID-19 pandemic, new variants of the SARS-CoV-2 virus, such as the omicron variant, continue to pose significant challenges, affecting individuals not only with acute COVID-19 disease but also leading to a condition known as long-COVID.[1]

Long-COVID is characterized by a range of persistent symptoms, including respiratory issues, cardiovascular symptoms, and cognitive impairments such as brain fog, fatigue, insomnia, and memory problems.[2] However, our understanding of long-COVID remains limited due to the scarcity of suitable animal models for research. Developing precise animal models replicating the pathophysiological aspects of long-COVID is essential for advancing our knowledge and finding effective therapeutic solutions.

The infectivity of SARS-CoV-2 hinges on its interaction with the angiotensin-converting enzyme 2 (ACE2) receptor, primarily mediated by its spike protein. Selecting appropriate animal models for COVID-19 research depends on accurately replicating this interaction. While some animals, like golden hamsters and ferrets, are naturally susceptible to SARS-CoV-2, their mild symptoms and limited research resources make them less ideal for studying severe disease outcomes.[3] Non-human primates, which display more human-like symptoms, present ethical and logistical challenges.[4] Mice, the most commonly used laboratory animals, typically exhibit low-affinity ACE2 binding to SARS-CoV-2. Although mouse-adapted strains of the virus have been developed, they do not fully represent the spectrum of viral variants.[3]

One widely used model, K18-hACE2 mice, express human ACE2 in epithelial cells under the human cytokeratin 18 promoter (K18) and exhibit severe symptoms after SARS-CoV-2 infection.[5] However, limitations include co-expression of both mouse and human ACE2 and a high mortality rate, making conducting prolonged studies post-infection recovery challenging. Therefore, a novel mouse model closely mirroring human COVID-19 symptoms is required. In pursuit of this goal, several studies have developed and utilized new hACE2 knock-in (KI) mouse models.[6,7] Yet, these experiments mainly focused on confirming infection status with a single viral strain, with limited comparisons between different variants and short observation periods up to 7 days after infection. Notably, the impact of SARS-CoV-2 infection on long-COVID has not been reported using these mouse lines.

In this study, we introduce a novel humanized ACE2 mouse model created by replacing mouse *Ace2* exons 1–9 with full-length human ACE2 cDNA, preceded by a loxp-stop-loxp

cassette enabling genetic manipulation through the Cre-loxp system. This unique mouse model offers advantages distinct from existing humanized ACE2 mouse models, allowing for the study of SARS-CoV-2 infection's impact systemically or in specific tissues. We have validated a global humanized ACE2 mouse model by cross-breeding the floxed human ACE2 with Ella-Cre mice and confirmed their susceptibility to SARS-CoV-2 variants. Furthermore, our research delves into the potential link between SARS-CoV-2 infection and neurodegenerative diseases, such as Alzheimer's disease (AD), by examining tau pathology and its correlation with ACE2 localization in the mouse brain. Our newly generated hACE2ki mouse line is a valuable tool for studying viral tropism, investigating the pathogenesis of long-COVID or post-acute COVID sequelae (PASC), and exploring preventive and therapeutic strategies.

Results

Generation and Characterization of Novel Humanized ACE2 (hACE2ki) Mouse Line

In our efforts to investigate the pathogenesis of SARS-CoV-2 infection and its long-term effects and to assess potential interventional strategies for COVID-19 and related diseases, we have developed a novel humanized ACE2 mouse line, namely, hACE2ki. Employing CRISPR/Cas9 technology, we replaced exons 1 to 9 of the mouse *Ace2* gene (mACE2) with the complete coding sequence (CDS) of human *ACE2* (hACE2), as shown in Figure 1A. This modification allowed us to maintain the promoter region of mACE2, thus driving the expression of the substituted hACE2 in a manner consistent with the native mouse gene.

Additionally, the inserted hACE2 sequence includes a loxp-stop-loxp domain positioned upstream of the CDS. This feature enables us to regulate hACE2 expression through breeding with transgenic mice that carry Cre recombinase. For our current study, we generated hACE2ki mice in which hACE2 is expressed in all tissues or cells where the mouse *Ace2* promoter is active by cross-breeding floxed hACE2ki mice with EIIaCre transgenic mice, which express Cre recombinase in a wide range of tissues, as depicted in Supplementary Figure 1A.

To validate the expression of the hACE2 gene in hACE2ki mice, we conducted RT-qPCR to detect human *ACE2* or mouse *Ace2* gene expressions in tissue samples from the intestine, kidney, lung, liver, heart, and brain of both hACE2ki and wild-type (WT) mice. Figures 1B and 1C illustrate that the most abundant *ACE2* and *Ace2* expressions are in the intestines, followed by relatively high levels in the kidneys, lungs, and livers. The expressions in the hearts and brains are comparatively lower. These results confirm a shared expression pattern of *ACE2* in hACE2ki mice and *Ace2* in WT mice, substantiating that the mouse *Ace2* promoter effectively drives human ACE2 expression in the hACE2ki mice. Notably, the mouse *Ace2* gene was undetectable in hACE2ki mice (see Supplementary Figure S1C), underscoring the sole functional presence of human ACE2.

Further, to confirm the alignment of human ACE2 protein expression and cell lineage association with that of mouse ACE2, we selectively conducted immunofluorescence staining for human or mouse ACE2 (IF) in lung sections of both hACE2ki and WT mice. The results, presented in Figures 1D and 1E, show that both mouse and human ACE2

proteins are primarily abundant in the airways. To delineate the cell type-specific ACE2 protein expression pattern, we co-stained ACE2 with respective cell lineage markers: SPC (type II pneumocyte), PDPN (type I pneumocyte), CC10 (club cell), and FOXJ1 (ciliated airway epithelia). As demonstrated in Figures 1F–M, we observed co-localization between ACE2 and SPC^+ type 2 alveolar cells in distal lungs (Figures 1F, 1J, indicated by yellow arrows). However, there was little or no ACE2 co-localization with $PDPN^+$ Type 1 alveolar cells (Figures 1G, 1K). Notably, in the airway and proximal lungs, high ACE2 expression was observed in $CC10^+$ club cells and $FOXJ1^+$ ciliated cells (Figures 1H, 1I, 1L, 1M). These observations validate that human ACE2 is expressed and distributed in hACE2ki mice in a manner that closely mimics mouse ACE2 in WT mice.

hACE2ki Mice Inoculated with SARS-CoV-2 Variants Display Distinct Infectivity Patterns

To evaluate the susceptibility of hACE2ki mice to various SARS-CoV-2 strains, we intranasally inoculated 6-week-old mice with SARS-CoV-2 variants: WA (B.1), Delta (B.1.617.2), and Omicron (B.1.1.529), each at a dose of 5×10^5 Plaque Forming Units (PFU) per mouse. We monitored body weight and temperature daily, and mice were euthanized on days 1, 3, 6, 14, and 21 post-infection (dpi) for tissue collection (Figure 2A, Supplementary Figure S2A).

The hACE2ki mice infected with WA, Delta, and Omicron variants showed slight weight loss at 1 dpi, fully recovering by 2–3 dpi. In contrast, WT mice infected with the Mu strain experienced prolonged weight loss, most significant at 2 dpi, recovering fully by 9 dpi (Figure 2B, Supplementary Figure S2B). This pattern suggests milder symptoms in hACE2ki mice compared to the commonly used K18-hACE2 mice which do not survive beyond 7 dpi even with a lower dose of 2×10^4 PFU of SARS-CoV-2 WA (Supplementary Figure S2D). No significant changes in body temperature were observed in hACE2ki and WT mice infected with SARS-CoV-2 (Figure 2C, Supplementary Figure S2C), unlike K18-hACE2 mice, which showed a significant drop in temperature from 5 dpi (Supplementary Figure S2E).

Viral replication dynamics were assessed by measuring viral RNA in the lungs and converting qPCR Ct values for the SARS-CoV-2 N1 gene to genome equivalent units/ml using a standard curve (Supplementary Figure S3). The SARS-CoV-2 titer peaked at 1 dpi in hACE2ki mice infected with WA and Delta strains. Omicron-infected hACE2ki mice showed a peak at 1 dpi but with a lower detectable viral RNA than other lineages (Figure 2D), while the peak viral load is at 3 dpi in Mu-infected WT mice (Supplementary Figure S2F).

We also examined the impact of viral infection by different viral strains on *ACE2* expression in the lungs of hACE2ki mice. Infections with WA and Delta strains and Mu in WT mice led to a slight decrease in human ACE2 expression at 1 dpi, followed by a rebound around 4 dpi, peaking at 21 dpi. In contrast, Omicron infection in hACE2ki mice caused only mild variations in gene expression, except for an increase at 6 dpi (Figure 2E, Supplementary Figure S2G), suggesting an infection-associated dynamic in ACE2 expression post SARS-CoV-2 infection.

To investigate whether lung infection by SARS-CoV-2 variants in hACE2ki mice spreads to other tissues, we screened for viral presence using qRT-PCR in various tissues at 3 dpi. Results showed that virus genome signals were detectable in the lung, turbinate, and trachea in all mice inoculated with the three virus strains. Notably, the Delta strain demonstrated higher infectivity, with detectable viral RNA in the brain and heart (Figure 2G). In contrast, the Omicron strain showed the lowest distribution of viral RNA, observed only in the lung and turbinate (Figure 2H). These findings establish that hACE2ki mice can attract various SARS-CoV-2 strains and display distinct virus replication profiles.

Differential Host Immune Responses in hACE2ki Mice to SARS-CoV-2 Variants.

Given the varied infectivity patterns observed in hACE2ki mice inoculated with different SARS-CoV-2 variants, we explored whether these differences correlate with distinct host immune responses, a common phenomenon in COVID-19 patients. Our primary focus was on the variants' potential to induce inflammatory responses, a hallmark of COVID-19, often characterized by a cytokine storm.

We first conducted RT-qPCR to assess the expression dynamics of critical cytokines and chemokines in the lung, brain, and heart tissues of hACE2ki mice infected with SARS-CoV-2 variants at various post-inoculation intervals. As depicted in Figure 3, the levels of interferon-gamma (IFNγ), interferon-alpha (IFNα), and interleukin-6 (IL-6) in the lungs did not change significantly up to 14 dpi for all three variants. However, the Delta variant uniquely induced a sustained elevation in IFNγ expression, peaking at 14 dpi and continuing to 21 dpi. In contrast, infection with the Omicron variant resulted in the most substantial increase in IFNα expression at 21 dpi (Figure 3A).

We noted variant-specific cytokine expression patterns in the brain at particular time points. The WA strain induced the highest IFNγ expression at 3 dpi, and IFNα levels remained elevated post-infection, peaking at 21 dpi. The Omicron variant, however, showed relatively low cytokine expression levels overall, with a notable increase in IFNγ expression at 1 dpi. The brain of hACE2ki mice infected with the Delta variant did not exhibit a consistent cytokine pattern, suggesting unique variant-driven inflammatory responses in the brain, even though no specific cytokine stood out significantly among the three variants (Figure 3B).

In the heart, similar to the lungs, WA and Delta lineages caused an increase in cytokine expression at 21 dpi. Interestingly, the heart tissue of mice infected with the Omicron lineage showed a significant decrease in cytokine expression at 3 and 6 dpi, followed by recovery (Figure 3C). The above observation indicates variant-specific cytokine expression in the heart as well.

Further investigations into the gene expressions of IP-10 and TNFα did not reveal any clear patterns between different variants or cytokines (Supplementary Figure S4A–C). A detailed comparison of cytokine expression among the variants is provided in Supplementary Figure S4D.

We next assessed the immune cell infiltration in the lungs of hACE2ki mice infected with various SARS-CoV-2 lineages by using flow cytometric analysis to examine immune cell

populations in bronchoalveolar lavage fluid (BALF). Our findings revealed a significant infiltration of dendritic cells, neutrophils, macrophages, B cells, and T cells into the lungs, reaching a peak at 3 dpi for all three SARS-CoV-2 variants (Figure 4A–G). Intriguingly, dendritic cells, macrophages, and B cells showed a secondary peak in infiltration at 14 dpi (Figure 4A, 4C, 4D).

A key observation was that the Delta variant, which demonstrated the highest viral RNA loads among the three tested lineages, induced the most significant immune cell infiltration at 3 dpi. In contrast, the Omicron variant, characterized by the lowest lung viral RNA loads, led to the most robust induction of immune cell infiltration at 14 dpi. This finding indicates a clear correlation between virus lineage and immune cell infiltration patterns in our mouse model.

The comprehensive profile of immune cells infiltrating the lungs of mice infected with the different SARS-CoV-2 variants is presented in Supplementary Figure S5A–G. The gating strategy used for the flow cytometric analysis is detailed in Table S3 and Supplementary Figure S4H.

SARS-CoV-2 Infection-Induced Tau Pathology and ACE2 Correlation in Multiple Brain Regions of hACE2ki Mouse Model

Despite our humanized hACE2ki mouse line not displaying severe disease progression when inoculated with various SARS-CoV-2 variants at a young adult age, we aimed to assess its suitability for investigating long-COVID or Post-Acute Sequelae of SARS-CoV-2 infection pathogenesis and potential interventions. A key focus was to determine if SARS-CoV-2 infection in this model leads to tau pathologies, a known indicator for neurological disorders and a suggested long-term consequence of SARS-CoV-2 infection.[8–13]

Recent investigations have revealed increased hyperphosphorylated tau181 (p-tau181) in individuals afflicted with SARS-CoV-2 infection[14] and during the convalescence phase following COVID-19 infection.[15] This particular variant of hyperphosphorylated tau 181 has been identified as a specific biomarker associated with AD.[16] Despite the absence of definitive causal links between SARS-CoV-2 infection and AD,[14,17–20] the examination of pre-clinical mouse models presents a valuable opportunity to gain crucial insights into the relationship between SARS-CoV-2 and AD. SARS-CoV-2 infection has been documented to induce hyperphosphorylated tau (p-tau) pathology in various models, encompassing human neuronal cell lines,[21] human neurons,[22] as well as in animal subjects such as Syrian golden hamsters,[23] K18-hACE2 and C57BL/6J mice.[7] Given the well-established connection between tau pathology and cognitive dysfunction in AD,[24,25] it is paramount to investigate the development of SARS-CoV-2-induced tau pathology within brain regions linked to cognitive function using pre-clinical mouse models.[26,27] The ACE2 receptor plays a pivotal role in facilitating SARS-CoV-2 infection[28], and its involvement has also been associated with neuropathological changes in AD mouse models.[26,27] Hence, there is a compelling rationale for exploring the potential correlation between ACE2 receptor expression and the development of tau pathology, which could yield novel insights into the pathogenesis of AD in the context of SARS-CoV-2 infection.

Therefore, we conducted extensive tau pathology examinations by immunostaining for hyperphosphorylated tau 202/205 (clone: AT8) in the cortex, hippocampus, striatum, and amygdala. Our results indicate that in hACE2ki mice infected with the SARS-CoV-2 WA variant, a significant increase in AT8 immunoreactivity was observed in the cortex at 14 dpi compared to mock-infected controls (Figure 5A, B), using ACE2 knockout ($ACE2^{-/-}$) mice as a negative control. We also evaluated ACE2 receptor expression in infected and uninfected hACE2ki mice, finding no significant variance at 14 dpi (Figure 5C). A robust positive correlation (Pearson correlation coefficient of 0.8079) was found between AT8 immunoreactivity and ACE2 expression in the cortex following infection (Figure 5D).

We further examined tau pathology, ACE2 receptor expression, and their correlation in the hippocampus, striatum, and amygdala, which are critical for cognitive functions. In these regions, SARS-CoV-2 infection in hACE2ki mice at 14 dpi induced notable tau pathology, unlike in uninfected hACE2ki and $ACE2^{-/-}$ mice (Figure 5E, F, I, J, M, N). ACE2 expression in these brain regions of infected hACE2ki mice was comparable to non-infected mice (Figure 5G, K, O). Strong positive correlations between ACE2 receptor expression and tau pathology were confirmed, with Pearson correlation coefficients of 0.8299 in the hippocampus, 0.8425 in the striatum, and 0.7730 in the amygdala.

The above observations in hACE2ki mice are mirrored in WT mice infected with the Mu variant of SARS-CoV-2 at 14 dpi (Supplementary Figure. S6).

A possible co-localization of AT8 positive signal with SARS-CoV-2 spike protein staining is observed (Supplementary Figure S7), implying a potential viral infection *per se-induced* tau pathology.

Temporal Progression of Tau Pathology and ACE2 Expression in SARS-CoV-2-Infected Mouse Brain

Acknowledging the progressive nature of tau pathology over time,[29,30] we extended our assessment to monitor its progression in the cortex at various time points post-SARS-CoV-2 infection, including days 1, 3, 6, 9, 14, and 21 (Figure 6A, B). We observed a significant increase in AT8-positive immunoreactivity from day 3 to day 21, compared to day 0. However, the difference between day 1 and day 0 was not substantial (Figure 6A, B). This pattern suggests a gradual, time-dependent increase in tau pathology in the cortex following SARS-CoV-2 infection.

Simultaneously, we evaluated ACE2 receptor expression over this timeframe and found no significant variations at different time points (Figure 6A, C). Correlation analyses between ACE2 intensity and AT8 immunoreactivity were conducted to explore their relationship over time. Initially, the correlation was moderate on days 3 and 6 (Pearson correlation coefficients of 0.3602 at day 3 and 0.4675 at day 6). However, a notable increase in the correlation strength was observed on days 14 and 21 (Pearson correlation coefficients of 0.8166 on day 14 and 0.8938 on day 21), indicating a strengthening association between ACE2 expression and tau pathology as the infection progressed.

Similarly, in the hippocampus, tau pathology progressively increased post-SARS-CoV-2 infection (Figure 6H, I), while ACE2 expression remained consistent over time (Figure 6H, J). Specifically, AT8-positive immunoreactivity from day 6 to 21 was significantly higher than at day 0, but no significant changes were noted on days 1 and 3 compared to day 0 (Figure 6H, I). This observation indicates an earlier onset of tau pathology in the cortex than in the hippocampus in SARS-CoV-2-related AD trajectory. Our correlation studies underscored the time-dependent linear relationship between ACE2 expression and AT8 intensity (Figure 6K, L, M, N).

Our study confirms the expression of hACE2 in the brains of hACE2ki mice and establishes a clear link between SARS-CoV-2 infection and the progressive development of tau pathology. These findings provide crucial insights into the pathogenesis of SARS-CoV-2 infection-related AD trajectory, highlighting the dynamic interplay between ACE2 expression and tau pathology over time. Most importantly, our observations validate the suitability of our hACE2ki mouse line in long-COVID or PASC related investigations.

Discussion

Our study introduces the hACE2ki mouse line, created using CRISPR/Cas9 technology to integrate the human *ACE2* gene into the mouse genome. This novel humanized model, featuring a lox-stop-lox cassette ahead of the human CDS, is regulated by the native mouse *Ace2* promoter (Figure 1A). This strategic design allows for targeted expression of human *ACE2* in specific tissues and cells, making it a more physiologically relevant platform for studying SARS-CoV-2 pathogenesis and potential therapeutic strategies. The alignment of human *ACE2* expression in hACE2ki mice with mouse *Ace2* in WT mice (Figure 1B, 1C) underscores its potential for exploring human-specific disease mechanisms, particularly those involving ACE2.

There are two common strategies for studying COVID-19 in mouse models. The first involves using mouse-adapted mutant viruses, which exhibit a higher affinity for mACE2 due to mutations in the SARS-CoV-2 receptor binding domain,[31] However, these adapted viruses may not accurately represent the pathogenesis of existing and emerging viral strains. The second strategy uses genetically modified mice with human ACE2 expression, such as the K18-hACE2 model. Despite its utility, the K18-hACE2 model bears shortcomings from limitations like overexpression in specific cell types and high mortality rates not reflective of human infection. Although several humanized ACE2 mouse lines are available[3,32], our newly generated humanized ACE2 mouse model adapts a loxP-stop-loxP sequence at the front of the hACE2 CDS, enabling the human ACE2 expression in selected tissues or cells, and the expression is driven by native mouse promoter. In the current study, the floxed hACE2 mice cross-bred with Ellacre mice (Supplementary Figure S1A). The newly created hACE2ki mice express human *ACE2* in infected mouse lungs by different variants with different patterns, which mirror Mu strain viral infection in WT mice, confirming that human *ACE2* expression is precisely driven by mouse *Ace2* promoter. Notably, a diminished ACE2 expression in early stages of SARS-CoV-2 infection in hACE2ki mice, parallel observations in COVID-19 patients.[33] This model, therefore, has the potential to serve as a critical tool in accurately reflecting human disease progression and immune

responses, contributing significantly to advancing our understanding of SARS-CoV-2 infection dynamics.

The expression of ACE2 in the lung is known to vary with age.[34] In the current study, we utilized young adult hACE2ki mice aged around 6 weeks, where ACE2 expression is predominantly concentrated in the airway. In contrast, older mice often exhibit a more widespread distribution of ACE2 expression throughout various lung regions, including distal areas. This age-related variation in ACE2 expression could potentially influence our study's observed mild phenotype following SARS-CoV-2 infection, aligning with findings reported in other research.[34–47] Our ongoing investigations, which include mice of various ages, aim to elucidate these age-related differences in immune responses to viral infection.

Clinical phenotypes specific to different viral strains have been well documented. Notably, infections with the Delta variant are associated with a higher risk of severe lung disease, whereas the Omicron variant typically results in milder symptoms.[48] In our study, the Delta variant, in particular, showed evidence of superior infectivity, with detectable viral particles in the brain and heart at 3 dpi. This finding corroborates clinical reports and validates our newly created hACE2ki mouse model as an effective tool for COVID-19 research that accurately reflects human disease.

Our model also revealed an association between viral infectivity and pro-inflammatory cytokine levels. The most pronounced cytokine and chemokine responses were observed in the lungs of mice infected with the Delta variant, whereas the Omicron variant elicited the slightest response. This pattern mirrors clinical data that have identified strain-specific severity in cytokine storms, correlating with significant differences in mortality among patients infected with various SARS-CoV-2 strains. These observations confirm that our hACE2ki mouse model resembles phenotypes observed in human patients, highlighting its suitability for comprehensive COVID-19 studies.

The phenomenon of immune cell infiltration into the lungs during SARS-CoV-2 infection is well-documented in existing literature.[49,50] Consistent with these studies, our research observed significant infiltration of various immune cells, including B cells, T cells, dendritic cells, neutrophils, and macrophages, into the lungs at 3 dpi. This early immune response is crucial to the host's defense against viral infections.

Notably, most previous studies have focused on short-term infections, typically up to 7 dpi, leaving the immune cell composition during the recovery phase largely uncharted. In our study, we extended the observation period to 21 dpi, allowing us to monitor the dynamics of immune cell populations in the BALF beyond the acute phase of infection. Intriguingly, we noted a resurgence in the numbers of B cells, dendritic cells, and macrophages at 14 dpi (Figure 4B, 4D, 4E), which correlates strongly with the cytokine expression patterns observed in Figure 3A.

This finding suggests that the impact of the virus on the immune system persists even after the virus is no longer detectable, potentially influencing the immune response for an extended period. Such prolonged immune activation could contribute to the development of long-COVID symptoms. This observation underscores the complexity of the immune

response to SARS-CoV-2 infection. It highlights the importance of considering long-term immune dynamics in understanding and managing COVID-19, particularly in the context of long-COVID.

The extended duration of our study provides new insights into the post-acute phase of SARS-CoV-2 infection, a critical period that has been relatively under-researched. Understanding these prolonged immune responses is vital for developing effective strategies to prevent and treat long-term complications associated with COVID-19.

The implications of these findings are substantial. They suggest that our hACE2ki mouse model effectively mimics human disease pathogenesis in adaptive immunity, particularly in the context of variant-specific immune responses. This model, therefore, provides a valuable platform for studying the nuances of humoral immunity in COVID-19, enhancing our understanding of how different viral strains interact with the immune system. Such insights are crucial for developing effective vaccines and therapies, especially considering the emergence of new SARS-CoV-2 variants.

Furthermore, previous studies have established that tau proteins interact with membrane lipids, crucial in AD and other neurodegenerative disorders.[51] Therefore, the observed expression of AT8 due to SARS-CoV-2 infection suggests a potential link between SARS-CoV-2 infection and AD. In this study, we have found reasonable evidence for increased tau pathology during SARS-CoV-2 infection. However, how SARS-CoV-2 infection increases tau pathology in the brain is unclear. As visualizing ACE2 expression in the brain has proven a correlation between ACE2 expression and tau pathology when compared with control samples, the infected samples showed a significant increase in ACE2 expression and tau pathology in various areas of the brain. The mechanism by which SARS-CoV-2 aids in the propagation of pathogenic tau in the brain may not be apparent; however, it has been shown previously that infection by multiple pathogens, whether they are bacterial or viral, leads to increased aggregation of amyloidogenic proteins, as seen in the case of respiratory syncytial virus (RSV) and the herpes simplex virus (HSV-1).[52] There is evidence of brain-barrier inflammation in COVID-19.[53] In the same study, it was found that the inflamed choroid plexus relayed inflammatory signals into the brain, resulting in impairment of cognitive function after SARS-CoV-2 infection, although not directly.[53] Impaired cognitive function is also a result of increased amyloid aggregation in the brain. We found that the most significant signal of tau pathology was detected in the cortex, followed by the hippocampus, striatum, and amygdala. Tau pathology was found to be increased with the duration of infection. On comparing tau pathology between samples infected with dpi 1 and those infected with dpi 14, we observed more significant tau pathology in samples infected with dpi 14. We found a strong correlation between ACE2 expression and tau pathology. Other brain regions, including the hippocampus, striatum, and amygdala, also showed a strong correlation between ACE2 and AT8 expression. The results showed that tau immunoreactivity is positively correlated with the intensity of ACE2 in the SARS-CoV-2 infected mice.

We found evidence of SARS-CoV-2 in the brain by detecting the spike protein of SARS-CoV-2 in samples infected with SARS-CoV-2. Neural cells can be prone to infection by

the virus as they contain the ACE2 receptor. However, low levels of the ACE2 gene expression may indicate that only a small population of neural cells express ACE2 and can, therefore, be infected by the virus.[54] ACE2 was upregulated five-fold in the tissues obtained from autopsy of AD patients versus the controls.[55] In another study, it was found that SARS-CoV-2 viral antigens were confined to the neurons of the vagal nuclei of the medulla and the substantia nigra.[56] Of note, ACE2 was found to be upregulated in the tissues obtained from autopsy of AD patients,[39] which may indicate that dpi 21 is not long enough to observe the dynamic ACE2 expression.

In summary, we created a novel hACE2ki mouse model to conduct acute and long COVID-19-related research detailing the distinct pathogenesis, disease progression, and intervention strategies. Using young adult mice, this model exhibited mild symptoms similar to those experienced by most patients, underscoring its suitability as a pre-clinical animal model for investigating COVID-19 caused by emerging viral strains and the long-COVID. However, there were some limitations observed in our study. The absence of detectable viral load in the trachea of Omicron-infected mice contrasts with the results of patients showing mainly the upper airway as a target.[57] Moreover, the high variability observed in lung-infiltrating immune cells among mice required a larger number of mice per group to ensure accurate experiments. Considering these limitations and employing our model thoughtfully, our new mouse model can serve as an excellent tool for studying ACE2 expression, viral infection, and inflammatory responses. We anticipate that this model will provide valuable research data on various SARS-CoV-2 variants and help us understand the pathology of the long-COVID.

Methods

Generation and characterization of humanized ACE2 mouse line (hACE2ki).

We newly generated the hACE2ki transgenic mice from C57BL/B6 background for this study. The generation process began with the pronuclear injection of one-cell C57BL/6J embryos (Jackson Laboratories), executed by the JHU Transgenic Core. The standard microinjection technique, as described by Nagy A et al. (2003), was employed. The injection mix comprised Cas9 protein (30ng/μl, IDT), tracrRNA (0.6μM, IDT), crRNA (0.6μM, IDT), and ssDNA template (5ng/μl, Genewiz), all diluted in RNAse-free injection buffer (10 mM Tris-HCl, pH 7.4, 0.25 mM EDTA).

Injected embryos were transferred into the oviducts of pseudo-pregnant ICR females (Charles River), utilizing the technique from Nagy A et al. (2003). Guide RNAs targeting exon 1 through exon 9 of the mouse *Ace2* gene were employed, with primer sequences detailed in Table S1. The replacement template, designed to replace mouse exons 1 to 9 with the human ACE2 CDS preceded by a lox-stop-lox sequence (Addgene, 51269), was also utilized.

The first generation (F0) offspring underwent genotyping using two specific primers, hACE2Kki 3’ and hACE2Kki 5’ (Table S1), to confirm the correct insertion of intact the human ACE2 sequence. The expected PCR product sizes were 321bp for hACE2ki 3’ and

305bp for hACE2Kki 5'. Genotype-positive mice were backcrossed with wild-type (WT) mice to produce the F1 generation.

These mice were crossed with Ella Cre mice to activate hACE2 expression through excision of the lox-stop-lox sequence. The homozygous hACE2Kki mice used in this experiment were bred for five additional generations. Before the experiments, DNA samples from hACE2-positive mice were genotyped to confirm the presence of the hACE2Kki and the absence of mACE2 (KO) using the hACE2Kki-ko primer. Off-target effects were assessed using the mACE2intron4 primer. The expected PCR product sizes were 300bp for the mACE2ko, 1208bp for WT with the hACE2Kki -ko primer, and 466bp for the mACE2intron4 primer. Primer sequences are listed in Table S1, and the resulting gel electrophoresis band images are presented in Supplementary Figure 1B.

Experimental Procedures Involving Animals and Viruses

All mouse experiments adhered to protocols approved by the JHU animal care and use committee (Protocol number MO22M280). The C57BL/B6 mice and K18-hACE2 were procured from The Jackson Laboratory. Global ACE2 knockout ($ACE2^{-/-}$) mice were generously provided by Dr. J. Penninger from the Life Sciences Institute, University of British Columbia.

Mice were administered a light dose of ketamine/xylazine and intranasally infected with 5×10^5 PFU of SARS-CoV-2 Mu (SARS-CoV-2/USA/MD-HP06587/2021; B.1.621; GISAID EPI_ISL_3243079), WA (SARS-CoV-2/USA-WA1/2020; A.1; BEI Resources, NR#52281), Delta (SARS-CoV-2/USA/MD-HP05660/2021; AY.106; GISAID EPI_ISL_2331507), and Omicron (SARS-CoV-2/USA/MD-HP20874/2021; BA.1.18; GISAID EPI_ISL_7160424) variants in 50 μl of DMEM. Body weight and temperature were monitored daily. Mice were sacrificed for analysis on 1, 3-, 6-, 14, and 21 days post-infection. For comparison, WT mice were inoculated with the SARS-CoV-2 Mu (B.1.621) strain, known to infect C57BL/6 mice at the same age and dose. All SARS-CoV-2 experiments were conducted in an ABSL3 facility at Johns Hopkins University.

RNA Extraction and qRT-PCR:

Mouse tissues were homogenized, and total RNA was extracted using Trizol. For each sample, 1 μg of RNA was used for cDNA synthesis using the High-Capacity Reverse Transcription Kit (Applied Biosystems). Real-time quantitative PCR was performed using iTaq Universal SYBR Green Supermix (Bio-Rad) on the Bio-Rad CFX96 system. Transcript abundance was normalized to GAPDH and presented as $2^{-\Delta Ct}$, using specific primers listed in Table S1.

Viral Load Determination:

Standard curves for SARS-CoV-2 N1 genes were generated by plotting Ct values against PFU to calculate viral load in the tissues as genome equivalent units. The virus stock was diluted from 1×10^4 to 2×10^7 PFU/ml, and qPCR was performed using nCOV_N1 (FAM) Probe Aliquot (IDT) and SsoAdvanced Universal Probes Supermix (Bio-Rad). The

primers used were nCOV_N1 Forward and Reverse Primers (IDT). The standard curve (Supplementary Figure 2C) was used to interpolate tissue virus titer results.

Immunofluorescence analysis of lung section

Lung tissues were harvested from the mice and immediately fixed with 4% paraformaldehyde (PFA) in phosphate-buffered saline (PBS). Dehydration, washing, and paraffinization were performed on the Tissue processor. The samples were embedded in paraffin using a tissue embedding station. Samples were then sectioned at 5 μm and put on positively charged glass slides. The slides were deparaffinized and rehydrated in ethanol (100%, 95%, and 70%). The samples were processed for antigen retrieval in citrate buffer (10 mM, pH 6) for immunofluorescence staining. Samples were then washed with PBS blocked with 1% bovine serum albumin (BSA) in PBS for 1hr at room temperature (RT). After washing, the slides were incubated overnight at 4°C with primary antibodies diluted in 1% BSA in PBS (1:200). The primary antibodies used for staining are listed in Table S2 and washed three times with 0.5% BSA in PBS, incubated with appropriate fluorescent-labeled secondary antibodies (Table S2) and the DAPI for nuclear staining, then mounted using Gelvatol solution before imaging using a fluorescence microscope (Leica). To enhance co-localization visualization, the colors of SPC, PDPN, CC10, and FOXJ1 were changed to red using ImageJ software for analysis.

Immunofluorescence analysis of brain section

Brains were collected and incubated with 4% PFA for at least 24 hours at 4°C. The brain was transferred to a 15 ml conical tube containing 30% sucrose in PFA and incubated until the brain sank to the bottom of the tube (~ 72h). The 30 μm coronal slices were obtained using a sliding microtome (Thermo Scientific, HM450). Brain sections were blocked in with 5% goat serum with 0.3% Triton X-100 for 1h at RT and then incubated overnight at 4 °C with mice Phospho-Tau (Ser202, Thr205) Monoclonal Antibody (AT8) antibody (dilution 1:1,000) as primary antibody for tau pathology assay or anti-mACE2 antibody (dilution1:1000) or anti-hACE2 antibody (dilution1:1000) for ACE2 expression. Incubation with secondary antibodies such as anti-rabbit IgG conjugated to Alexa-fluor 568 (1:1000 dilution), anti-mouse IgG conjugated to Alexa-fluor 488 (1:1000 dilution), and Hoechst (1:5000 dilution) for 1h at RT. Slides were prepared, and images were acquired on a fluorescence microscope (Zeiss Axio Observer Z1) and then analyzed with Zen Lite software and ImageJ. The areas with low to high degrees of ACE2 expression were selected for quantification and quantified for AT8 and ACE2 signals using ImageJ—quantification of the AT8 and ACE2 immunoreactivity normalized by Hoechst. Pearson correlation analysis was performed using GraphPad Prism.

ELISA for Mouse Immunoglobulin:

An indirect ELISA was conducted using SARS-CoV-2 spike protein (Sino biological) to measure IgG and IgM levels in mouse serum. Following overnight antigen coating and subsequent blocking, serum samples and detection antibodies were added. The enzymatic reaction was initiated using a substrate solution (R&D systems), and OD at 450 nm was measured.

Flow Cytometry of BALF:

BALF was obtained post-euthanasia, and cells were processed for flow cytometry analysis. After blocking Fc receptors and staining with fluorescent-conjugated antibodies (Table S2), samples were analyzed on a Northern Lights flow cytometer (Cytek), with data processed using Flowjo software. The gating strategy is outlined in Table S3.

Supplementary Material

Refer to Web version on PubMed Central for supplementary material.

Acknowledgements:

We thank Mr. Chip Hawkins of Transgenic Mouse Core of Johns Hopkins University School of Medicine for his technical support and dedication to generating humanized ACE2 mouse lines. We appreciate Mr. Thomas Prindle for maintaining mouse colonies. We acknowledge the support from The Multiphoton Imaging Core of Johns Hopkins University was used (NS050274) in some of the imaging studies.

Funding:

NIH 1R2AI14932101 (HJ), 3R21AI149321-01S1 (HJ), and 1R01AI148446-01A1 (HJ), NIH R01AG073291 (XM), CurePSP Venture Grant 658-2018-06 (XM), AFAR New Investigator Award in Alzheimer's disease (XM), R01NS107318 (XM), P50 AG05146 Pilot Project ADRC (XM).

References

1. Antonelli M, Pujol JC, Spector TD, Ourselin S & Steves CJ Risk of long COVID associated with delta versus omicron variants of SARS-CoV-2. Lancet 399, 2263–2264 (2022). 10.1016/S0140-6736(22)00941-2 [PubMed: 35717982]
2. Perumal R et al. Long COVID: a review and proposed visualization of the complexity of long COVID. Front Immunol 14, 1117464 (2023). 10.3389/fimmu.2023.1117464 [PubMed: 37153597]
3. Jia H, Yue X & Lazartigues E ACE2 mouse models: a toolbox for cardiovascular and pulmonary research. Nat Commun 11, 5165 (2020). 10.1038/s41467-020-18880-0 [PubMed: 33057007]
4. Shou S et al. Animal Models for COVID-19: Hamsters, Mouse, Ferret, Mink, Tree Shrew, and Non-human Primates. Front Microbiol 12, 626553 (2021). 10.3389/fmicb.2021.626553 [PubMed: 34531831]
5. Golden JW et al. Human angiotensin-converting enzyme 2 transgenic mice infected with SARS-CoV-2 develop severe and fatal respiratory disease. JCI Insight 5 (2020). 10.1172/jci.insight.142032
6. Kim SH et al. Mouse models of lung-specific SARS-CoV-2 infection with moderate pathological traits. Front Immunol 13, 1055811 (2022). 10.3389/fimmu.2022.1055811 [PubMed: 36457995]
7. Sun SH et al. A Mouse Model of SARS-CoV-2 Infection and Pathogenesis. Cell Host Microbe 28, 124–133 e124 (2020). 10.1016/j.chom.2020.05.020 [PubMed: 32485164]
8. Amalakanti S, Arepalli KVR & Jillella JP Cognitive assessment in asymptomatic COVID-19 subjects. Virusdisease 32, 146–149 (2021). 10.1007/s13337-021-00663-w [PubMed: 33614860]
9. Brown RL et al. Pathophysiology, diagnosis, and management of neuroinflammation in COVID-19. BMJ 382, e073923 (2023). 10.1136/bmj-2022-073923 [PubMed: 37595965]
10. de Erausquin GA et al. Chronic neuropsychiatric sequelae of SARS-CoV-2: Protocol and methods from the Alzheimer's Association Global Consortium. Alzheimers Dement (N Y) 8, e12348 (2022). 10.1002/trc2.12348 [PubMed: 36185993]
11. Javed A Neurological Associations of SARS-CoV-2 Infection: A Systematic Review. CNS Neurol Disord Drug Targets 21, 246–258 (2022). 10.2174/1871527320666210216121211 [PubMed: 33593267]
12. Nakamura ZM, Nash RP, Laughon SL & Rosenstein DL Neuropsychiatric Complications of COVID-19. Curr Psychiatry Rep 23, 25 (2021). 10.1007/s11920-021-01237-9 [PubMed: 33725218]

13. Wan D et al. Neurological complications and infection mechanism of SARS-COV-2. Signal Transduct Target Ther 6, 406 (2021). 10.1038/s41392-021-00818-7 [PubMed: 34815399]
14. Frontera JA et al. Comparison of serum neurodegenerative biomarkers among hospitalized COVID-19 patients versus non-COVID subjects with normal cognition, mild cognitive impairment, or Alzheimer's dementia. Alzheimer's & Dementia 18, 899–910 (2022). 10.1002/alz.12556
15. Sun B et al. Characterization and Biomarker Analyses of Post-COVID-19 Complications and Neurological Manifestations. Cells 10 (2021). 10.3390/cells10020386
16. Janelidze S et al. Plasma P-tau181 in Alzheimer's disease: relationship to other biomarkers, differential diagnosis, neuropathology and longitudinal progression to Alzheimer's dementia. Nat Med 26, 379–386 (2020). 10.1038/s41591-020-0755-1 [PubMed: 32123385]
17. Reiken S et al. Alzheimer's-like signaling in brains of COVID-19 patients. Alzheimers Dement 18, 955–965 (2022). 10.1002/alz.12558 [PubMed: 35112786]
18. Ding Q & Zhao H Long-term effects of SARS-CoV-2 infection on human brain and memory. Cell Death Discov 9, 196 (2023). 10.1038/s41420-023-01512-z [PubMed: 37380640]
19. Granholm AC Long-Term Effects of SARS-CoV-2 in the Brain: Clinical Consequences and Molecular Mechanisms. J Clin Med 12 (2023). 10.3390/jcm12093190
20. Heneka MT, Golenbock D, Latz E, Morgan D & Brown R Immediate and long-term consequences of COVID-19 infections for the development of neurological disease. Alzheimers Res Ther 12, 69 (2020). 10.1186/s13195-020-00640-3 [PubMed: 32498691]
21. Di Primio C et al. Severe acute respiratory syndrome coronavirus 2 infection leads to Tau pathological signature in neurons. PNAS Nexus 2, pgad282 (2023). 10.1093/pnasnexus/pgad282 [PubMed: 37731949]
22. Ramani A et al. SARS-CoV-2 targets neurons of 3D human brain organoids. EMBO J 39, e106230 (2020). 10.15252/embj.2020106230 [PubMed: 32876341]
23. Kaufer C et al. Microgliosis and neuronal proteinopathy in brain persist beyond viral clearance in SARS-CoV-2 hamster model. EBioMedicine 79, 103999 (2022). 10.1016/j.ebiom.2022.103999 [PubMed: 35439679]
24. James OG, Doraiswamy PM & Borges-Neto S PET Imaging of Tau Pathology in Alzheimer's Disease and Tauopathies. Front Neurol 6, 38 (2015). 10.3389/fneur.2015.00038 [PubMed: 25806018]
25. Nelson PT et al. Clinicopathologic correlations in a large Alzheimer disease center autopsy cohort: neuritic plaques and neurofibrillary tangles "do count" when staging disease severity. J Neuropathol Exp Neurol 66, 1136–1146 (2007). 10.1097/nen.0b013e31815c5efb [PubMed: 18090922]
26. Duan R et al. ACE2 activator diminazene aceturate ameliorates Alzheimer's disease-like neuropathology and rescues cognitive impairment in SAMP8 mice. Aging (Albany NY) 12, 14819–14829 (2020). 10.18632/aging.103544 [PubMed: 32701063]
27. Evans CE et al. ACE2 activation protects against cognitive decline and reduces amyloid pathology in the Tg2576 mouse model of Alzheimer's disease. Acta Neuropathol 139, 485–502 (2020). 10.1007/s00401-019-02098-6 [PubMed: 31982938]
28. Hoffmann M et al. SARS-CoV-2 Cell Entry Depends on ACE2 and TMPRSS2 and Is Blocked by a Clinically Proven Protease Inhibitor. Cell 181, 271–280 e278 (2020). 10.1016/j.cell.2020.02.052 [PubMed: 32142651]
29. Chen C et al. Pathological Tau transmission initiated by binding lymphocyte-activation gene 3. bioRxiv (2023). 10.1101/2023.05.16.541015
30. Guo JL et al. Unique pathological tau conformers from Alzheimer's brains transmit tau pathology in nontransgenic mice. J Exp Med 213, 2635–2654 (2016). 10.1084/jem.20160833 [PubMed: 27810929]
31. Sun S et al. Characterization and structural basis of a lethal mouse-adapted SARS-CoV-2. Nat Commun 12, 5654 (2021). 10.1038/s41467-021-25903-x [PubMed: 34580297]
32. Zhou B et al. SARS-CoV-2 spike D614G change enhances replication and transmission. Nature 592, 122–127 (2021). 10.1038/s41586-021-03361-1 [PubMed: 33636719]

33. Gutierrez-Chamorro L et al. SARS-CoV-2 Infection Modulates ACE2 Function and Subsequent Inflammatory Responses in Swabs and Plasma of COVID-19 Patients. Viruses 13 (2021). 10.3390/v13091715
34. Inde Z et al. Age-dependent regulation of SARS-CoV-2 cell entry genes and cell death programs correlates with COVID-19 severity. Sci Adv 7 (2021). 10.1126/sciadv.abf8609
35. Abrehart T et al. Age-related differences in SARS-CoV-2 binding factors: An explanation for reduced susceptibility to severe COVID-19 among children? Paediatr Respir Rev 44, 61–69 (2022). 10.1016/j.prrv.2022.01.008 [PubMed: 35227628]
36. Berni Canani R et al. Age-Related Differences in the Expression of Most Relevant Mediators of SARS-CoV-2 Infection in Human Respiratory and Gastrointestinal Tract. Front Pediatr 9, 697390 (2021). 10.3389/fped.2021.697390 [PubMed: 34395341]
37. Bloise E et al. Expression of severe acute respiratory syndrome coronavirus 2 cell entry genes, angiotensin-converting enzyme 2 and transmembrane protease serine 2, in the placenta across gestation and at the maternal-fetal interface in pregnancies complicated by preterm birth or preeclampsia. Am J Obstet Gynecol 224, 298 e291–298 e298 (2021). 10.1016/j.ajog.2020.08.055
38. Chen J et al. Individual variation of the SARS-CoV-2 receptor ACE2 gene expression and regulation. Aging Cell 19 (2020). 10.1111/acel.13168
39. Ding Q, Shults NV, Gychka SG, Harris BT & Suzuki YJ Protein Expression of Angiotensin-Converting Enzyme 2 (ACE2) is Upregulated in Brains with Alzheimer's Disease. Int J Mol Sci 22 (2021). 10.3390/ijms22041687
40. Ding Q, Shults NV, Harris BT & Suzuki YJ Angiotensin-converting enzyme 2 (ACE2) is upregulated in Alzheimer's disease brain. bioRxiv (2020). 10.1101/2020.10.08.331157
41. Inde Z et al. Age-dependent regulation of SARS-CoV-2 cell entry genes and cell death programs correlates with COVID-19 disease severity. bioRxiv (2020). 10.1101/2020.09.13.276923
42. Lu M, Qiu L, Jia G, Guo R & Leng Q Single-cell expression profiles of ACE2 and TMPRSS2 reveals potential vertical transmission and fetus infection of SARS-CoV-2. Aging (Albany NY) 12, 19880–19897 (2020). 10.18632/aging.104015 [PubMed: 33104520]
43. Maremanda KP, Sundar IK, Li D & Rahman I Age-Dependent Assessment of Genes Involved in Cellular Senescence, Telomere, and Mitochondrial Pathways in Human Lung Tissue of Smokers, COPD, and IPF: Associations With SARS-CoV-2 COVID-19 ACE2-TMPRSS2-Furin-DPP4 Axis. Front Pharmacol 11, 584637 (2020). 10.3389/fphar.2020.584637 [PubMed: 33013423]
44. Papadopoulos KI, Papadopoulou A & Aw TC A protective erythropoietin evolutionary landscape, NLRP3 inflammasome regulation, and multisystem inflammatory syndrome in children. Hum Cell 36, 26–40 (2023). 10.1007/s13577-022-00819-w [PubMed: 36310304]
45. Rodrigues R & Costa de Oliveira S The Impact of Angiotensin-Converting Enzyme 2 (ACE2) Expression Levels in Patients with Comorbidities on COVID-19 Severity: A Comprehensive Review. Microorganisms 9 (2021). 10.3390/microorganisms9081692
46. Seeland U et al. Evidence for treatment with estradiol for women with SARS-CoV-2 infection. BMC Med 18, 369 (2020). 10.1186/s12916-020-01851-z [PubMed: 33234138]
47. Yee M, Cohen ED, Haak J, Dylag AM & O'Reilly MA Neonatal hyperoxia enhances age-dependent expression of SARS-CoV-2 receptors in mice. bioRxiv (2020). 10.1101/2020.07.22.215962
48. Suryawanshi RK et al. Limited cross-variant immunity from SARS-CoV-2 Omicron without vaccination. Nature 607, 351–355 (2022). 10.1038/s41586-022-04865-0 [PubMed: 35584773]
49. Kim S-H et al. Mouse models of lung-specific SARS-CoV-2 infection with moderate pathological traits. Frontiers in Immunology 13 (2022). 10.3389/fimmu.2022.1055811
50. Winkler ES et al. SARS-CoV-2 infection of human ACE2-transgenic mice causes severe lung inflammation and impaired function. Nat Immunol 21, 1327–1335 (2020). 10.1038/s41590-020-0778-2 [PubMed: 32839612]
51. El Mammeri N, Gampp O, Duan P & Hong M Membrane-induced tau amyloid fibrils. Commun Biol 6, 467 (2023). 10.1038/s42003-023-04847-6 [PubMed: 37117483]
52. Ezzat K et al. The viral protein corona directs viral pathogenesis and amyloid aggregation. Nat Commun 10, 2331 (2019). 10.1038/s41467-019-10192-2 [PubMed: 31133680]

53. Yang AC et al. Dysregulation of brain and choroid plexus cell types in severe COVID-19. Nature 595, 565–571 (2021). 10.1038/s41586-021-03710-0 [PubMed: 34153974]

54. Bullen CK et al. Infectability of human BrainSphere neurons suggests neurotropism of SARS-CoV-2. ALTEX 37, 665–671 (2020). 10.14573/altex.2006111 [PubMed: 32591839]

55. Piekut T et al. Infectious agents and Alzheimer's disease. J Integr Neurosci 21, 73 (2022). 10.31083/j.jin2102073 [PubMed: 35364661]

56. Emmi A et al. Detection of SARS-CoV-2 viral proteins and genomic sequences in human brainstem nuclei. NPJ Parkinsons Dis 9, 25 (2023). 10.1038/s41531-023-00467-3 [PubMed: 36781876]

57. Nori W & Ghani Zghair MA Omicron targets upper airways in pediatrics, elderly and unvaccinated population. World J Clin Cases 10, 12062–12065 (2022). 10.12998/wjcc.v10.i32.12062 [PubMed: 36405264]

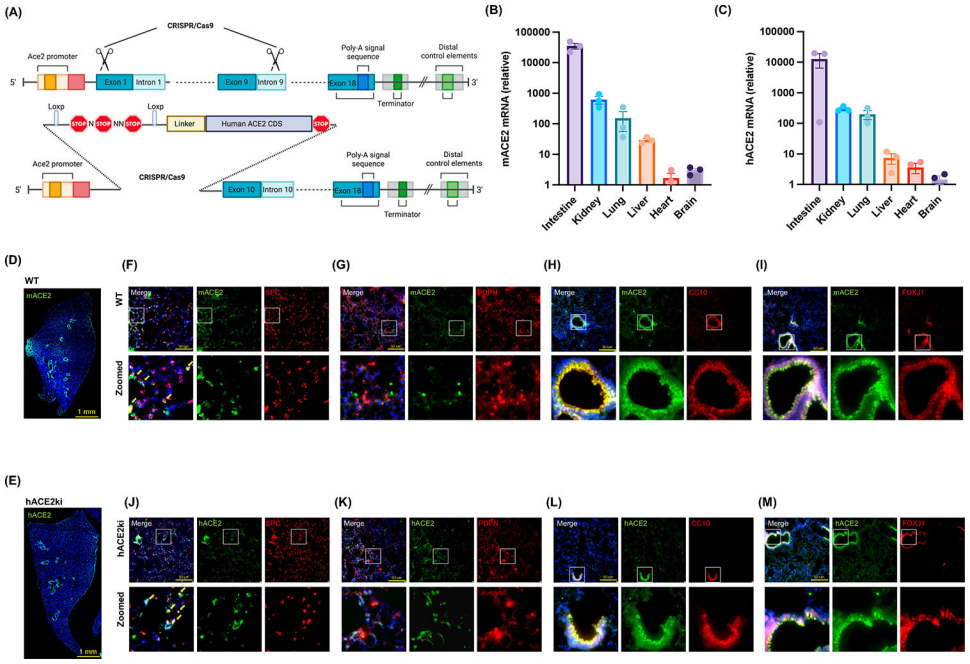

FIGURE 1. Generation and Characterization of Humanized ACE2 Mouse Line (hACE2ki)

(**A**) Schematic of hACE2ki mice generation, utilizing guide RNAs targeting exons 1–9 of mouse Ace2 gene and a replacement template for human *ACE2* CDS preceded by a lox-stop-lox sequence. (**B, C**) Comparative qPCR analysis of Ace2 (**B**) and human *ACE2* (**C**) mRNA expression across various tissues in WT and hACE2ki mice. (**D, E**) Immunofluorescence staining of lung sections for mouse (**D**) and human (**E**) ACE2 (green) in WT and hACE2ki mice, counterstained with DAPI (blue); Scale bar, 1 mm. (**F-M**) Co-localization studies in lung sections for mouse (**F-I**) and human (**J-M**) ACE2 (green) with cell markers SPC, PDPN, CC10, FOXJ1 (red), and DAPI (blue); Scale bar, 50 μm; higher magnification of framed areas shown.

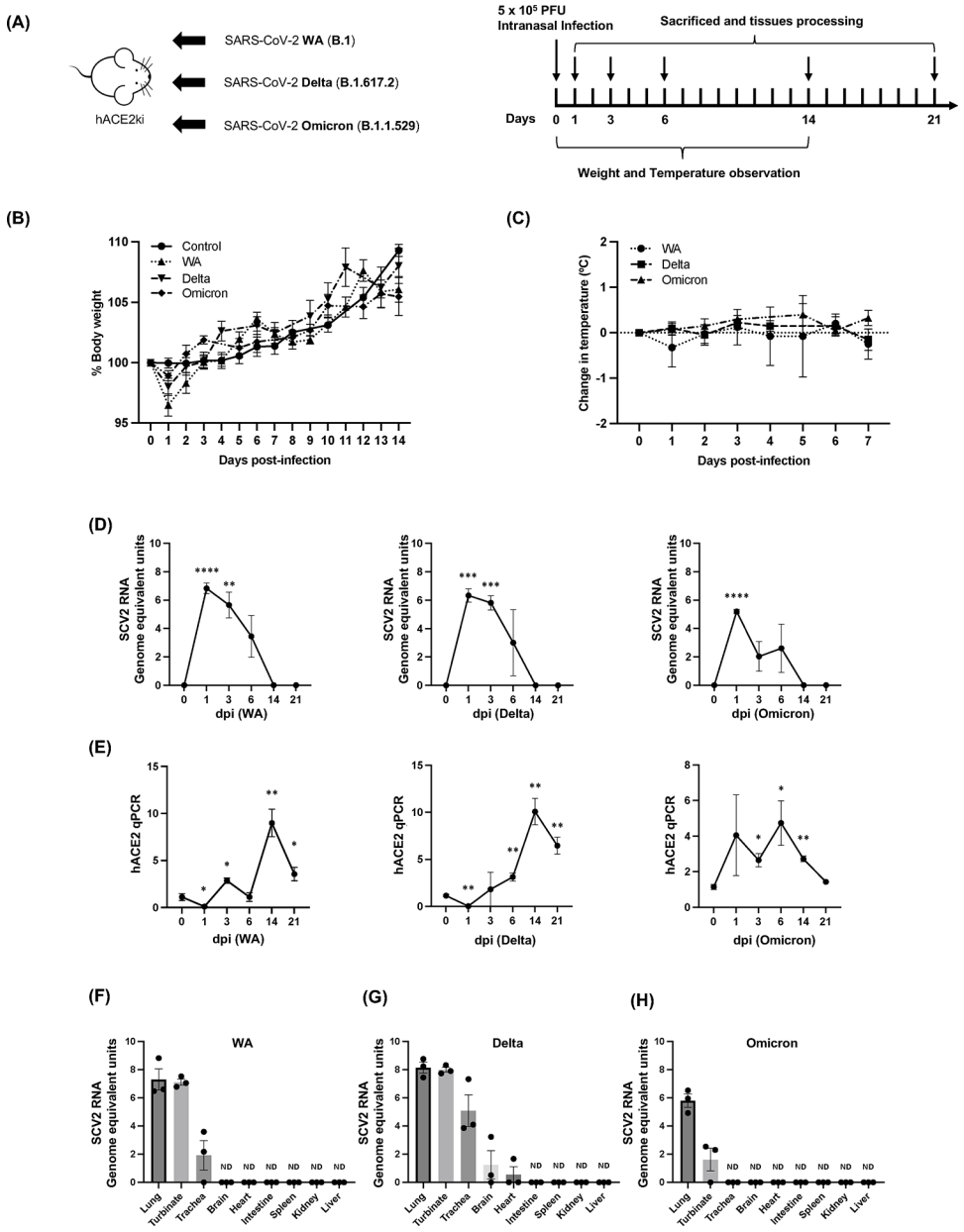

FIGURE 2. Infection of hACE2ki Mice with SARS-CoV-2 Variants

(**A**) Experimental design for intranasal infection of hACE2ki mice with 5×10^5 PFU of SARS-CoV-2 variants. (**B**) Body weight changes following SARS-CoV-2 variant infection. (**C**) Body temperature variations post-infection with SARS-CoV-2 variants. (**D**) Lung viral loads post-infection, quantified by qRT-PCR and converted to genome equivalent units. (**E**) Changes in lung ACE2 mRNA expression during infection, determined by qPCR. (**F-H**) Tissue-specific viral loads at 3 dpi with SARS-CoV-2 variants were assessed by qRT-PCR and converted to genome equivalent units. ND = not detected. *p<0.05, **p<0.01, ***p<0.001, ****p<0.0001. n≥4. Data are presented as the average ± s.e.m.

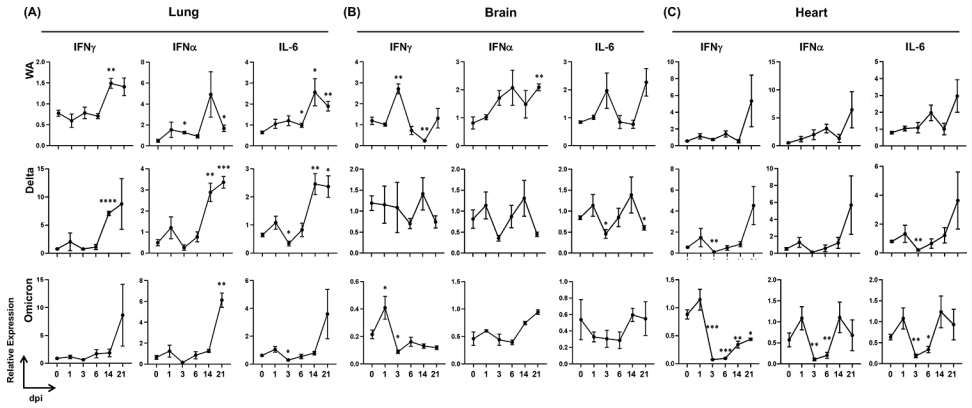

FIGURE 3. Cytokine and Chemokine Gene Expression in Lungs of SARS-CoV-2 Variant Infected Mice

(**A-C**) RT-qPCR analysis of cytokine and chemokine mRNA levels in lung (**A**), brain (**B**), and heart (**C**) from mice infected with WA, Delta, and Omicron variants. Data relative to 0 dpi; *p<0.05, **p<0.01, ***p<0.001, ****p<0.0001. n≥4. Data are presented as the average ± s.e.m.

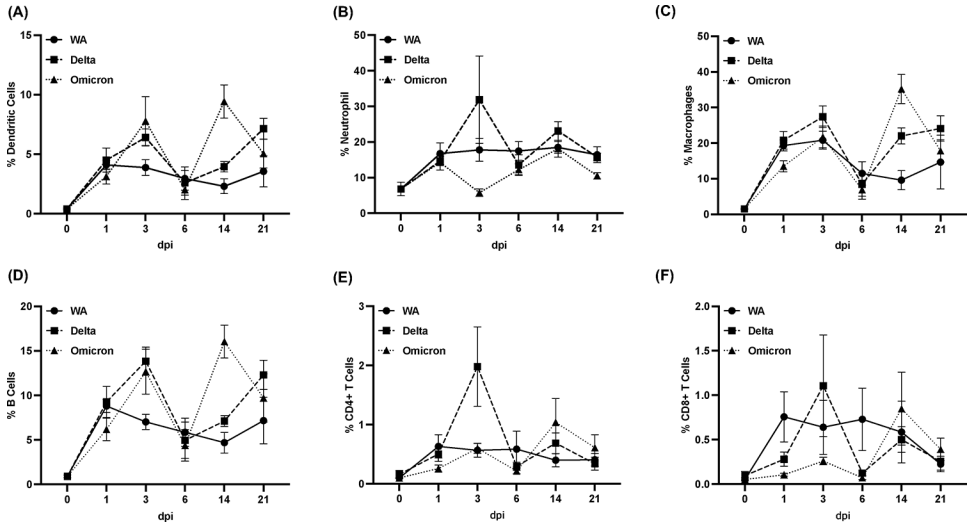

FIGURE 4. Immune Cell Profiling in BALF Post-SARS-CoV-2 Infection

(**A-F**) Flow cytometry measured the analysis of immune cell infiltration into the lungs post-infection with SARS-CoV-2 variants in BALF. Percentages of various cell lineages are shown. *p<0.05, **p<0.01, ***p<0.001. n≥4. Data are presented as the average ± s.e.m.

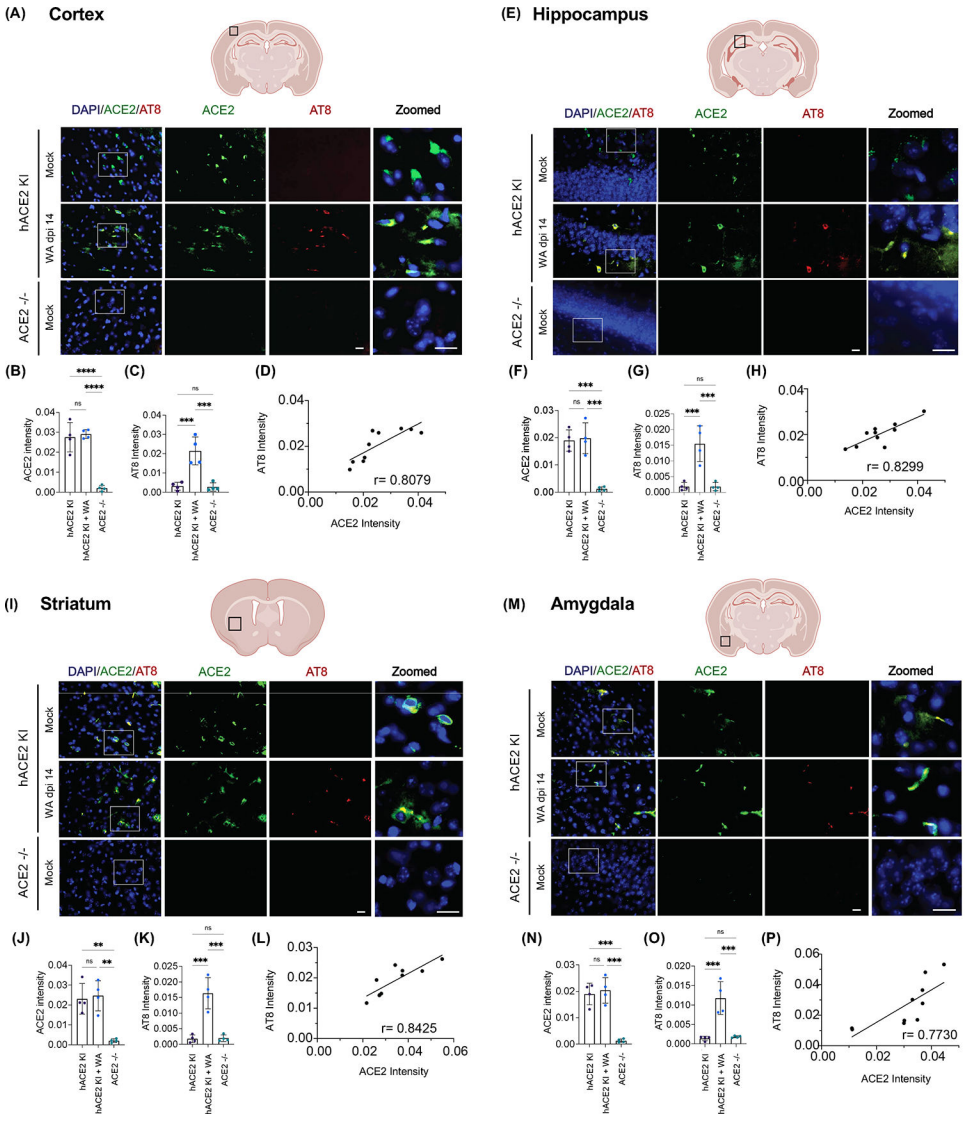

FIGURE 5. Correlation between ACE2 Expression and Tau Hyperphosphorylation in the Cortex and Associated Brain Regions during SARS-CoV-2 Infection in hACE2ki Mice at 14 days post-infection (dpi).

(A) Schematic depiction highlighting the analyzed cortical region (black box) and corresponding immunofluorescence images featuring ACE2 and AT8 immunostaining in hACE2 KI mice infected with SCV2-WA at 14 dpi. Negative controls included the hACE2 KI mock group and ACE2 knockout mice ($ACE2^{-/-}$). Scale bar, 20 μm. **(B, C)** Quantification of ACE2 **(B)** and AT8 **(C)** intensity. Normalization was performed relative to DAPI. **(D)** Correlation analysis of co-localized AT8 and ACE2 intensity in the cortex at 14 dpi, revealing a robust positive correlation (Pearson correlation coefficient r = 0.8079). Expression profiles of ACE2 and AT8 were also assessed in the hippocampus (**E, F, G**), striatum (**I, J, K**), and amygdala (**M, N, O**). (**H, L, P**) Robust positive correlations were observed between AT8 immunoreactivity and ACE2 expression in the hippocampus (r = 0.8299), striatum (r = 0.8425), and amygdala (r = 0.7730). N = 4 per group. Data are

presented as the average ± s.e.m. Significance levels: *p < 0.05, **p < 0.01, ***p < 0.001, ****p < 0.0001, with p-values determined using one-way ANOVA.

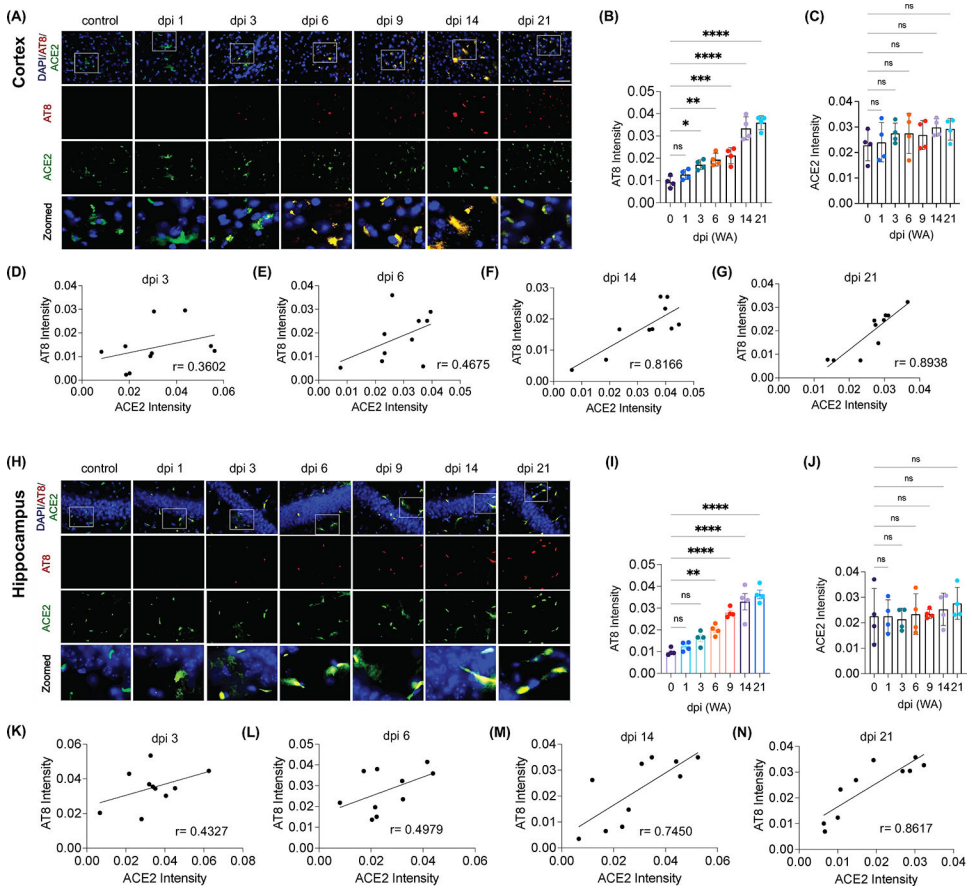

FIGURE 6. Temporal Analysis of ACE2 and AT8 Co-localization in hACE2ki Mice Cortex and Hippocampus during SARS-CoV-2 Infection.

Schematic depiction illustrating the analyzed cortical region (black box) and immunofluorescence images displaying ACE2 and AT8 staining in the cortex of hACE2 KI mice infected with SCV2-WA at multiple time points (1, 3, 6, 9, 14, 21 dpi). The negative control involves hACE2 without infection: scale bar, 20 μm. The quantification of AT8 (**B**) and ACE2 (**C**) intensity was normalized to DAPI. Correlation analysis of co-localized AT8 and ACE2 intensity in the cortex at 3 and 6 dpi, revealing a weak correlation (Pearson correlation coefficient r = 0.3602 and 0.4675). Correlation analysis at 14 and 21 dpi shows a robust positive correlation (Pearson correlation coefficient r = 0.8166 and 0.8938). Similar assessments were performed in the hippocampus for AT8 (**H, I**) and ACE2 (**H, J**) changes over time. Correlation analysis of co-localized AT8 and ACE2 intensity in the hippocampus at 3 and 6 dpi reveals a robust positive correlation (Pearson correlation coefficient r = 0.4327 and 0.4979), and correlation analysis at 14 and 21 dpi shows a robust positive correlation (Pearson correlation coefficient r = 0.7450 and 0.8617). N = 4 per group. Data are presented as the average ± s.e.m. Significance levels: *p < 0.05, **p < 0.01, ***p < 0.001, ****p < 0.0001, with p-values determined using one-way ANOVA.